Smart Structures and Systems, *Vol. 25, No. 2 (2020) 135-153*
DOI: https://doi.org/10.12989/sss.2020.25.2.135

Exploration of temperature effect on videogrammetric technique for displacement monitoring

Hua-Fei Zhou*[1], Lin-Jun Lu [1], Zhao-Yi Li [1] and Yi-Qing Ni [2]

[1] *College of Civil Engineering and Architecture, Wenzhou University, Wenzhou, China*
[2] *Department of Civil and Environmental Engineering, The Hong Kong Polytechnic University, Hong Kong*

(*Received January 27, 2019, Revised May 31, 2019, Accepted January 10, 2020*)

Abstract. There has been a sustained interest towards the non-contact structural displacement measurement by means of videogrammetric technique. On the way forward, one of the major concerns is the spurious image drift induced by temperature variation. This study therefore carries out an investigation into the temperature effect of videogrammetric technique, focusing on the exploration of the mechanism behind the temperature effect and the elimination of the temperature-caused measurement error. 2D videogrammetric measurement tests under monotonic or cyclic temperature variation are first performed. Features of measurement error and the casual relationship between temperature variation and measurement error are then studied. The variation of the temperature of digital camera is identified as the main cause of measurement error. An excellent linear relationship between them is revealed. After that, camera parameters are extracted from the mapping between world coordinates and pixels coordinates of the calibration targets. The coordinates of principle point and focal lengths show variations well correlated with temperature variation. The measurement error is thought to be an outcome mainly attributed to the variation of the coordinates of principle point. An approach for eliminating temperature-caused measurement error is finally proposed. Correlation models between camera parameters and temperature are formulated. Thereby, camera parameters under different temperature conditions can be predicted and the camera projective matrix can be updated accordingly. By reconstructing the world coordinates with the updated camera projective matrix, the temperature-caused measurement error is eliminated. A satisfactory performance has been achieved by the proposed approach in eliminating the temperature-caused measurement error.

Keywords: vision measurement system; structural displacement; environmental effect; temperature variation; structural health monitoring

1. Introduction

Videogrammetry is a measurement technique in which the coordinates of the points on an object are determined by the measurements made in video images (Surhone *et al.* 2010). In the last few decades, benefitting from the exceptional advances in image sensors, computers, as well as computer vision algorithms, videogrammetry has seen many advances. Its applications can be found in many diverse disciplines such as experimental mechanics (Sharpe Jr. 2008) and aerospace engineering (Liu *et al*. 2012), among others. Thanks to the non-contact nature, it has also allowed new opportunities for monitoring the displacement of a civil engineering structure. Accordingly, videogrammetric displacement monitoring has become the subject of intensive research in the civil engineering community over the past decades (Jiang *et al*. 2008, Baqersad *et al*. 2017, Feng and Feng 2018, Xu and Brownjohn 2018). A diversity of videogrammetric displacement monitoring techniques has been proposed and the applications in real civil engineering structures have also been reported (Olaszek 1999, Wahbeh *et al.* 2003, Lee *et al.* 2007, Chang and Xiao 2010, Lee *et al*. 2012, 2017, Busca *et al.* 2014, Feng and Feng 2016, Brownjohn *et al.* 2017, Feng and Feng 2017, Cho *et al*. 2018). As evidenced by previous studies, videogrammetric technique shows great potential in the field of civil engineering and it is being applied to an ever increasing range of tasks.

One of the major concerns in the applications of videogrammetric technique in field monitoring is the effect of temperature variation on the measurement accuracy. On one hand, the dark current, which is a noise source intrinsic to the image sensor, is strongly temperature dependent (Widenhorn *et al.* 2002). On the other hand, temperature variation will induce thermal deformation of the vision measurement system, which will lead to changes in camera parameters and thereby spurious drifts of image. It becomes more important as the potentials of the technique in structural health monitoring have gained more attention (Feng and Feng 2018). The ambient temperature will fluctuate significantly over a long time period, which may introduce intolerable errors into the measurement results. Nevertheless, limited studies on this topic have been reported in the literature. Robson *et al.* (1993) carried out an investigation into the suitability of CCD cameras for videogrammetric measurement. Image drift was observed during camera warm-up, which was referred to as warm-up effect. Handel (2009) focused on the study of the camera

*Corresponding author, Professor,
E-mail: mailtofei@wzu.edu.cn

http://www.techno-press.org/?journal=sss&subpage=7
ISSN: 1738-1584 (Print), 1738-1991 (Online)

warm-up effect on the image acquisition. He stated that the image drift was originated from a slight displacement of the image sensor due to the thermal expansion of camera mechanical components. Merchant (2006) performed calibration flights to study the influence of temperature variation on the focal length of an airborne camera. A change of focal length of 0.5 μm/°C was reported. Smith and Cope (2010) studied the effect of temperature variation on the parameters of a single-lens-reflex camera. The coordinates of principal point and focal length were shown to have a systematic relationship with temperature. The focal length changed by 1.0 μm/°C. Poulin-Girard *et al.* (2014) conducted virtual camera calibration simulations to study the variations of camera parameters at different temperatures of lens. The results showed changes in the focal length and distortion coefficients but not in the coordinates of principal point. Yu *et al.* (2014) investigated the effect of air temperature variation on the videogrammetric measurement. They argued that air temperature variation caused more significant and complicated changes in camera parameters than camera warm-up. Zhou *et al.* (2017) and Zhou *et al.* (2019) carried out videogrammetric measurement tests to study the temperature effect in non-laboratory environmental. A satisfactory linear relationship between displacement measurement error and temperature variation was revealed.

To eliminate the warm-up effect, Handel (2009) updated the time dependent camera extrinsic parameters with bi-exponential functions, supposing that the camera intrinsic parameters remained constant during the warm-up period. Likewise, Podbreznik and Potočnik (2012) proposed a modified camera model that takes account of the translation of a camera to eliminate temperature-caused error, assuming that the temperature variation does not affect the rest camera parameters. Nevertheless, those assumptions are inconsistent with the fact that camera intrinsic parameters have been shown to be prone to temperature variation. Yu *et al*. (2014) presented a temperature compensation method for a special case where the image plane is parallel to the world plane. They first established a simplified image drift model that correlated the drift of coordinates with the variation in camera parameters, and then formulated the correlation model between camera parameters and temperature variation. Rather than correcting temperature-caused image drift by means of updating camera parameters, Daakir *et al*. (2019) proposed to model the temperature-caused image drift with a 2D/3D spatial similarity transformation, which reflects the effect of the changing focal length and the translation and rotation of the image. The results showed that the variation of focal length was reproducible but not the variation of principle point and thereby the variation of focal length was modeled. To facilitate temperature compensation, Adamczyk *et al*. (2018) developed a modified camera design that exhibits a highly predictable behavior under varying ambient temperature. A fourth-degree polynomial was employed to model the temperature-caused image drift. The prototype of modified camera design needs to be improved and validated in real applications. As it can be seen, the existing temperature compensation methods usually make different, even contrary assumptions concerning the temperature-induced variability of camera parameters. It is therefore desirable to carry out a comprehensive study that uses a full camera model to investigate the temperature-induced variability of camera parameters. It not only will benefit the exploration of the mechanism responsible for the temperature effect, but also will help justify the simplified camera models proposed for temperature compensation.

This study carries out an investigation into the effect of temperature variation on the videogrammetric displacement measurement by focusing mainly on the exploration of the mechanism for the temperature effect and the elimination of the temperature-caused measurement error. First, 2D videogrammetric measurement tests, where fixed calibration targets are monitored by a vision measurement system, are conducted inside a room with air conditioning. Two scenarios of air temperature variation are considered, i.e., monotonic and cyclic temperature variations. Making use of the measurement data of displacement and temperature, features of measurement error and the casual relationship between temperature variation and measurement error are then revealed. After that, the underlying camera intrinsic and extrinsic parameters are extracted from the mapping between world and pixel coordinates of the calibration targets. By scrutinizing the temperature-induced variability of the camera parameters, the mechanism responsible for the temperature effect of the videogrammetric technique is explored. On this ground, an approach for eliminating the temperature-caused measurement error is proposed finally. Correlation models between camera parameters and temperature are formulated. Thereby, camera parameters at different temperature conditions are predicted, which are used to update the camera projective matrix. To eliminate the temperature-caused measurement error, the world coordinates of the target are reconstructed with the use of updated camera projective matrix. The performance of the proposed approach for eliminating the temperature-caused measurement error is examined by the measurement data acquired under cyclic temperature variation.

2. Theoretical background

2.1 Camera model

A camera model represents a camera mapping between the 3D world and a 2D image. To date, cameras modelling the central projection have been well recognized, and the same applies to this study. Assuming no optical distortion, a projective camera model can be represented as

$$s\mathbf{m} = \mathbf{PM} \tag{1}$$

where $\mathbf{M} = (X, Y, Z, 1)^{\mathrm{T}}$ is the homogeneous vector of a 3D point in the world coordinate system, $\mathbf{m} = (u, v, 1)^{\mathrm{T}}$ is the homogeneous vector of the corresponding 2D point in the pixel coordinate system, s is a scale factor, $\mathbf{P}$ is the camera projective matrix defined up to the scale factor with 11 degrees of freedom (DOFs). The direct linear transformation (DLT) method can be employed to solve for the camera projective matrix (Abdel-Aziz and Karara 2015).

The camera projective matrix encapsulates camera intrinsic and extrinsic parameters, which can be decomposed as

$$\mathbf{P} = \mathbf{K}[\mathbf{R}|\mathbf{T}] \tag{2}$$

with

$$\mathbf{K} = \begin{bmatrix} a_x & \gamma & u_0 \\ 0 & a_y & v_0 \\ 0 & 0 & 1 \end{bmatrix} \tag{3}$$

$$\mathbf{R} = [\mathbf{r}_1 \quad \mathbf{r}_2 \quad \mathbf{r}_3] = \begin{bmatrix} r_{11} & r_{12} & r_{13} \\ r_{21} & r_{22} & r_{23} \\ r_{31} & r_{32} & r_{33} \end{bmatrix} \tag{4}$$

$$\mathbf{T} = [t_x \quad t_y \quad t_z]^T \tag{5}$$

where $\mathbf{K}$ is the camera intrinsic matrix which represents the transformation from camera coordinate system to pixel coordinate system. It contains five parameters including the focal lengths in pixels a_x and a_y, the coordinates of principle point u_0 and v_0, and the skew parameter γ characterizing the skew of the two image axes, which is admittedly very unlikely to happen and thereby the skew parameter is usually zero. $\mathbf{R}$ is the rotation matrix and $\mathbf{T}$ is the translation vector, which together describe a rigid body transformation between world coordinate system and camera coordinate system. The rotation matrix $\mathbf{R}$ can also be expressed as

$$\begin{bmatrix} \cos\theta_y\cos\theta_z & \sin\theta_x\sin\theta_y\cos\theta_z - \cos\theta_x\sin\theta_z & \cos\theta_x\sin\theta_y\cos\theta_z + \sin\theta_x\sin\theta_z \\ \cos\theta_y\sin\theta_z & \sin\theta_x\sin\theta_y\sin\theta_z + \cos\theta_x\cos\theta_z & \cos\theta_x\sin\theta_y\sin\theta_z - \sin\theta_x\cos\theta_z \\ -\sin\theta_y & \sin\theta_x\cos\theta_y & \cos\theta_x\cos\theta_y \end{bmatrix} \tag{6}$$

where θ_x, θ_y and θ_z are the Euler angles which describe the orientation of a camera.

If all target points of interest lie on the same world plane, a simplified world coordinate system can be chosen such that $Z = 0$. Correspondingly, Eq. (1) can be reduced to

$$s\mathbf{m} = \mathbf{K}[\mathbf{r}_1\ \mathbf{r}_2|\boldsymbol{T}]\begin{bmatrix} X \\ Y \\ 1 \end{bmatrix} = \mathbf{H}\begin{bmatrix} X \\ Y \\ 1 \end{bmatrix} \tag{7}$$

where $\mathbf{H}$ is a homography matrix that transforms points on a world plane to the image plane. The homography matrix is also determined up to the scale factor and thereby has eight DOFs. Likewise, the DLT method can be employed to solve for the homography matrix as well.

Up to this point, it is assumed that the camera model is linear, which will not hold if there is lens distortion. Due to several types of imperfections in the design and assembly of lens, there often appears lens distortion. In general, there are three types of lens distortion, i.e., radial distortion, decentering distortion and thin prism distortion (Weng *et al.* 1992). Among them, the radial distortion has been proven to dominate the lens distortion. It has been reported that the modelling of radial distortion is quite sufficient even when high accuracy is required and the use of more complicated models not only would help but also would cause numerical instability (Salvi *et al.* 2002, Sun and Cooperstock 2006). Accordingly, only radial distortion is considered in this study, which is modelled as

$$\begin{aligned} \breve{x} &= x + \delta_{xr} \\ \breve{y} &= y + \delta_{yr} \end{aligned} \tag{8}$$

with

$$\begin{aligned} \delta_{xr} &= x[k_1(x^2+y^2) + k_2(x^2+y^2)^2] \\ \delta_{yr} &= y[k_1(x^2+y^2) + k_2(x^2+y^2)^2] \end{aligned} \tag{9}$$

where (x, y) is the ideal (non-observable distortion-free) image coordinates, $(\breve{x}, \breve{y})$ is the corresponding distorted (observed) image coordinates, δ_{xr} and δ_{yr} are the amount of radial distortion along x and y directions, k_1 and k_2 are the coefficients of radial distortion. The center of radial distortion coincides with the principal point. Correspondingly, Eqs. (8) and (9) can be expressed in pixel coordinates as

$$\begin{aligned} \breve{u} &= u + (u - u_0)[k_1(x^2+y^2) + k_2(x^2+y^2)^2] \\ \breve{v} &= v + (v - v_0)[k_1(x^2+y^2) + k_2(x^2+y^2)^2] \end{aligned} \tag{10}$$

where (u, v) and $(\breve{u}, \breve{v})$ are the ideal pixel coordinates and the corresponding distorted pixel coordinates. Combining Eq. (10) with Eq. (1) or (7), the coordinate transformation between distorted pixel coordinates and world coordinates can be determined, which is apparently nonlinear.

2.2 Camera calibration

Camera calibration is a necessary step in videogrammetric displacement measurement. So far, a variety of camera calibration methods have been reported in the literature (Salvi *et al.* 2002). As per the calibration target utilized, they can be classified as coplanar and non-coplanar approaches. Coplanar approaches perform calibration on targets limited to a planar surface of a single depth (Chatterjee and Roychowdhury 2000). They are often computationally complex and may fail to solve for some camera parameters. Non-coplanar approaches use targets scattered in 3D space to cover multiple depths (Weng *et al.* 1992, Faugeras and Toscani 1986, Tsai 1987). Usually, they involve an elaborate setup and require well-engineered calibration objects. To make the camera calibration more user friendly, Zhang (2000) developed a multi-planar calibration method that requires only planar calibration patterns positioned at a few different orientations. Thanks to the enhanced flexibility and a considerable degree of robustness, the method has been widely used now. Accordingly, this method is employed in this study, which is briefed as follows.

Denote the homography matrix $\mathbf{H}$ as

$$\mathbf{H} = [\mathbf{h}_1 \quad \mathbf{h}_2 \quad \mathbf{h}_3] = \begin{bmatrix} h_{11} & h_{12} & h_{13} \\ h_{21} & h_{22} & h_{23} \\ h_{31} & h_{32} & h_{33} \end{bmatrix} \tag{11}$$

Combining Eqs. (7) and (11) yields

$$\begin{aligned}\mathbf{r}_1 &= \mathbf{K}^{-1}\mathbf{h}_1\\ \mathbf{r}_2 &= \mathbf{K}^{-1}\mathbf{h}_2\\ \mathbf{T} &= \mathbf{K}^{-1}\mathbf{h}_3\end{aligned} \tag{12}$$

Applying the constraint that the column vectors of the rotation matrix $\mathbf{R}$ are orthonormal, i.e., ${\mathbf{r}_1}^{\mathrm{T}}\mathbf{r}_2 = 0$, $\|\mathbf{r}_1\| = \|\mathbf{r}_2\| = 1$, one gets

$$\begin{aligned}{\mathbf{h}_1}^T\mathbf{K}^{-T}\mathbf{K}^{-1}\mathbf{h}_2 &= 0\\ {\mathbf{h}_1}^T\mathbf{K}^{-T}\mathbf{K}^{-1}\mathbf{h}_1 &= {\mathbf{h}_2}^T\mathbf{K}^{-T}\mathbf{K}^{-1}\mathbf{h}_2\end{aligned} \tag{13}$$

Let

$$\mathbf{B} = \mathbf{K}^{-T}\mathbf{K}^{-1} \equiv \begin{bmatrix} B_{11} & B_{12} & B_{13}\\ B_{21} & B_{22} & B_{23}\\ B_{31} & B_{32} & B_{33}\end{bmatrix} \tag{14}$$

Making use of the symmetry of the matrix $\mathbf{B}$, which is apparent by recalling Eq. (3), one obtains

$${\mathbf{h}_i}^T\mathbf{B}\mathbf{h}_j = \mathbf{v}_{ij}^T\mathbf{b}\ (i = 1,2,3; j = 1,2,3) \tag{15}$$

with

$$\mathbf{v}_{ij} = \begin{bmatrix} h_{i1}h_{j1}, h_{i1}h_{j2} + h_{i2}h_{j1}, h_{i2}h_{j2,}h_{i3}h_{j1}\\ +h_{i1}h_{j3}, h_{i3}h_{j2} + h_{i2}h_{j3}, h_{i3}h_{j3}\end{bmatrix}^T \tag{16}$$

$$\mathbf{b} = [B_{11}, B_{12}, B_{22}, B_{13}, B_{23}, B_{33}]^T \tag{17}$$

Substituting Eq. (15) into Eq. (13) generates

$$\begin{bmatrix} \mathbf{v}_{12}^T\\ (\mathbf{v}_{11} - \mathbf{v}_{22})^T\end{bmatrix}\mathbf{b} = 0 \tag{18}$$

If the images of n world planes are observed, concatenating n such equation as (18) leads to

$$\mathbf{V}\mathbf{b} = 0 \tag{19}$$

where $\mathbf{V}$ is a $2n \times 6$ matrix. The vector $\mathbf{b}$ can be determined when $n \geq 3$, and thereby the matrix $\mathbf{B}$ can be obtained. After that, the intrinsic parameters can be extracted from matrix $\mathbf{B}$ as

$$\begin{aligned}&a_x = \sqrt{\lambda/B_{11}}\\ &a_y = \sqrt{\lambda B_{11}/(B_{11}B_{22} - {B_{12}}^2)}\\ &\gamma = -B_{12}{a_x}^2 a_y/\lambda\\ &u_0 = \gamma v_0/a_y - B_{13}{a_x}^2/\lambda\\ &v_0 = (B_{12}B_{13} - B_{11}B_{23})/(B_{11}B_{22} - {B_{12}}^2)\\ &\lambda = B_{33} - \left[{B_{13}}^2 + v_0(B_{12}B_{13} - B_{11}B_{23})\right]/B_{11}\end{aligned} \tag{20}$$

Once the intrinsic matrix $\mathbf{K}$ is determined, the 1st and 2nd column vector of the rotation matrix $\mathbf{R}$ as well as the translation vector $\mathbf{T}$ can be obtained from Eq. (12). Thanks to the orthogonality of the rotation matrix $\mathbf{R}$, its 3rd column can be computed as

$$\mathbf{r}_3 = \mathbf{r}_1 \times \mathbf{r}_2 \tag{21}$$

Recalling Eq. (6), the Euler angles θ_x, θ_y and θ_z can then be determined. Use the camera parameters computed without considering radial distortion as the initial guess, the coefficients of radial distortion can be obtained by the maximum likelihood estimation and the camera parameters are refined meanwhile. The maximum likelihood estimate can be obtained by minimizing the following cost function

$$\sum_{i=1}^{n}\sum_{j=1}^{m}\left\|\breve{\mathbf{m}}_{ij} - \widehat{\mathbf{m}}_{ij}(\mathbf{K}, k_1, k_2, \mathbf{R}_i, \mathbf{T}_i, \mathbf{M}_{ij})\right\|^2 \tag{22}$$

where $\mathbf{M}_{ij}$ is the jth point in the ith world plane, $\breve{m}_{ij}$ is the distorted (observed) projection of $\mathbf{M}_{ij}$ in the image plane, $\widehat{\mathbf{m}}_{ij}(\mathbf{K}, k_1, k_2, \mathbf{R}_i, \mathbf{T}_i, \mathbf{M}_{ij})$ is the estimated projection of $\mathbf{M}_{ij}$ obtained with the camera intrinsic matrix $\mathbf{K}$, coefficients of radial distortion k_1 and k_2, and rotation matrix $\mathbf{R}_i$ and translation vector $\mathbf{T}_i$ relative to the ith world plane. An initial guess of the coefficients of radial distortion k_1 and k_2 can be obtained by simply setting them to zero.

3. Experimental studies

3.1 Experimental setup

2D videogrammetric measurement tests, in which fixed calibration targets were monitored by a vision measurement system, were conducted inside a room with air conditioning. As there is still no consensus on the behavior of vision measurement system under varying temperature, extensive scenarios of temperature variation, including monotonic temperature drop, monotonic temperature rise, and cyclic temperature variation, were considered. The indoor air temperature was monitored in real time with a temperature sensor. Furthermore, temperatures of digital camera and zoom lens were monitored meanwhile. Four sensors were mounted on the digital camera with one on each of the four side surfaces. One sensor was attached on the side surface of the zoom lens. The temperature sensor has a resolution of 0.1°C. In addition, the illumination intensity, which may be another source of error, was monitored with a luminance sensor. To minimize the variation of illumination in the room, light emitting diode tube lights were turned on to provide stable illumination. Meanwhile, curtains were drawn across the windows to block out the sunlight. Throughout the tests, the indoor space was kept closed and uninterrupted by human activities.

Fig. 1 displays the experimental setup. The vision measurement system comprises a digital camera in conjunction with a zoom lens for image acquisition and a laptop for image processing. The digital camera is a monochrome 1/2” CCD with GigE vision interface. It has a resolution of 1024×1024 pixels and a maximum frame rate up to 60 fps. The zoom lens has the focal length ranging between 25 and 135 mm. They were placed on an optical platform of 800 mm high. The calibration target is the planar checkerboard pattern that consists of 12×9 black and white squares of equal size of 10×10 mm. It is printed on the quartz glass panel with a size of 150×120 mm. To be the

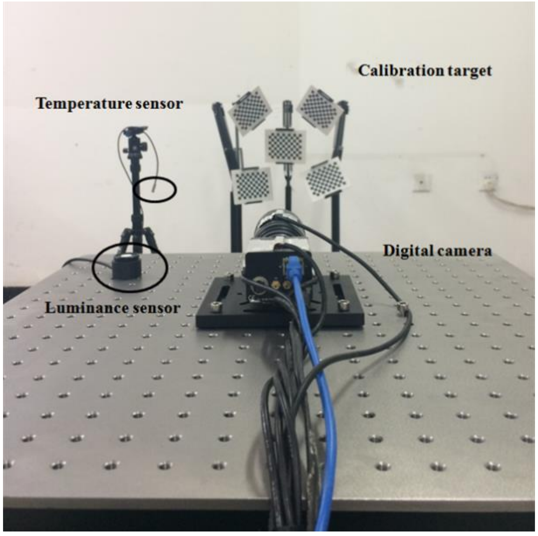

Fig. 1 Experimental setup

same height as the vision measurement system, the target panel was mounted on the stand. A total of five target panels with different orientations, which were kept fixed throughout the tests, were placed in front of the vision measurement system at a distance of some 1,800 mm. To make the vision measurement system, temperature measurement system and illumination intensity measurement system operate in synchronization, the clocks of the three systems were synchronized with the internet time server. The images were acquired at a frame rate of 2 fps; while the temperatures and illumination intensity were acquired at a sampling period of 1 minute.

One of the major concerns in the videogrammetric measurement tests is the virtual displacement that may be induced by the thermal deformation of the optical platform, target panels as well as their stands. Therefore, much effort has been made to minimize these thermal deformations. The target panel is made of quartz glass, which has a thermal expansion coefficient as small as 0.55×10^{-6}/°C. The optical platform and the stand are made of the same material of carbon fiber, which also has a small thermal expansion coefficient of -0.74×10^{-6}/°C. With a maximum temperature range of the air conditioner of 14°C, the thermal deformation of the target panel is less than 1 μm, and that of the optical platform and the stand is some 7 μm. It is therefore reasonable to maintain that the virtual displacement induced by the thermal deformation of the

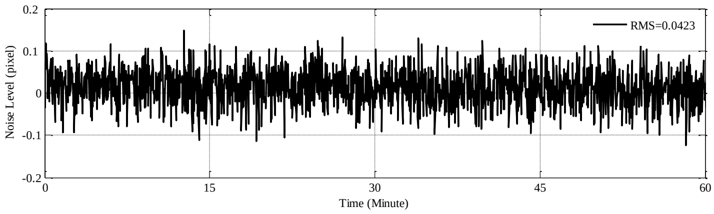

(a) Raw horizontal noise level

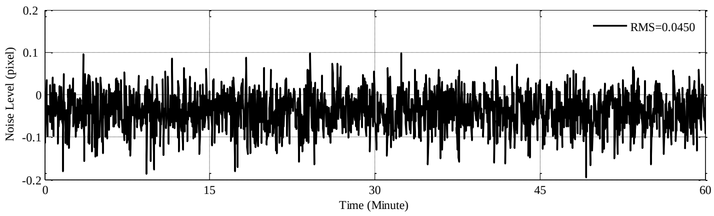

(b) Raw vertical noise level

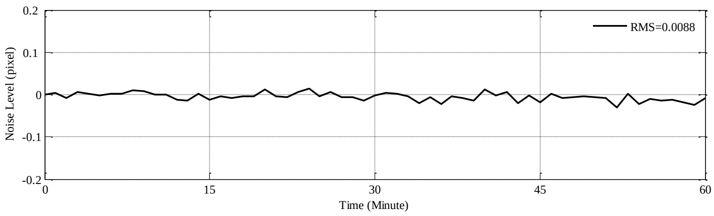

(c) 1-minute averaged horizontal noise level

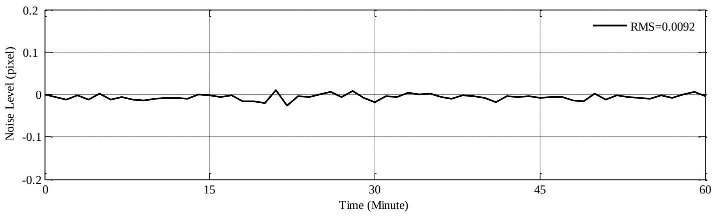

(d) 1-minute averaged vertical noise level

Fig. 2 Noise level in videogrammetric displacement measurement test optical platform, target panels and their stands is negligible. Meanwhile, the true values of the displacement of the corner could be thought of as zeros (the target panel was kept fixed throughout the tests), the measurement data could therefore be considered as displacement measurement errors purely. To obtain the measurement error, a corner detector exemplified by Geiger *et al.* (2012), which is capable to achieve sub-pixel accuracy, is employed to determine the pixel coordinates of the corners of the checkerboard pattern. With reference to the pixel coordinates in the initial frame, the displacement measurement error can then be obtained.

3.2 Experimental results

To determine the noise level in the videogrammetric displacement measurement tests, a preliminary test, in which the indoor air temperature was kept nearly constant, was first carried out. Fig. 2 plots the displacement measurement data of the (4,6) corner on central target panel. As it can be seen, the displacement randomly fluctuates around zero (the true values of the displacement are thought of as zeros), evidencing that the displacement measurement data are purely random noise. Notable random noise has been observed. Its root mean square (RMS) is more than 0.040 pixels in either horizontal or vertical direction. To eliminate the random noise, the displacement measurement data were averaged every one minute, which are also shown in Fig. 2. It is seen that the use of average minimizes the random noise substantially. The one minute averaged displacement is nearly zero, which squares with the fact. Meanwhile, the RMS of the random noise reduces to some 0.009 pixels. Therefore, the one minute averaged displacement is used hereafter so as to eliminate the random noise, unless otherwise specified.

The first test was performed when the indoor air temperature experienced monotonic drop and the corresponding measurement data were denoted as Dataset 1. Fig. 3 shows the indoor air temperature, temperatures of digital camera, temperature of zoom lens as well as illumination intensity in Dataset 1. In this period, the illumination intensity fluctuated in a small range between 222.1 and 225.5 lux, demonstrating that the illumination intensity kept almost constant. Under the action of an air conditioner, the indoor air temperature dropped from 27.8°C to 17.6°C. Consequently, the temperatures of vision

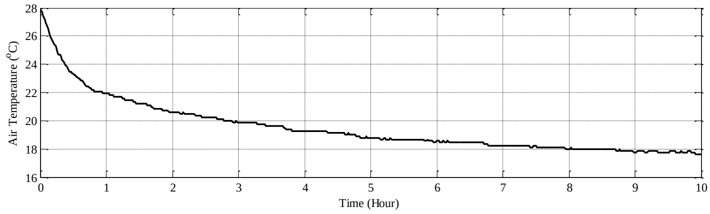

(a) Indoor air temperature

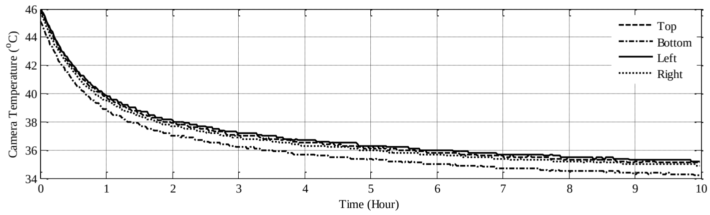

(b) Temperatures of digital camera

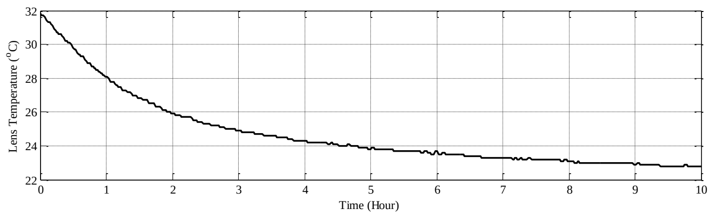

(c) Temperatures of zoom lens

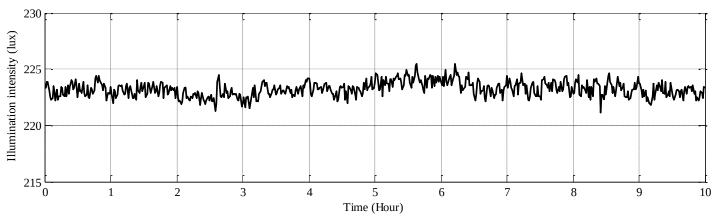

(d) Illumination intensity

Fig. 3 Indoor air temperature, temperatures of vision measurement system as well as illumination intensity in Dataset 1

Table 1 Correlation coefficients between temperatures of vision measurement system and indoor air temperature in Dataset 1

Temperatures of digital camera				Temperature of zoom lens
Top	Bottom	Left	Right	
0.994	0.994	0.994	0.994	0.986

measurement system, including those of digital camera and zoom lens, generally dropped in step with the indoor air temperature. To quantify the degree of correlation between temperatures of vision measurement system and indoor air temperature, their correlation coefficients were calculated and summarized in Table 1. All the correlation coefficients are more than 0.980, which demonstrates that the temperatures of vision measurement system are completely correlated with the indoor air temperature in this test.

As an illustration, Fig. 4 presents the measurement error of the (4,6) corner on central target panel in Dataset 1. Recalling Fig. 3, it is apparent that the measurement errors in both directions show a good agreement with temperature while they are almost uncorrelated with illumination intensity. As the temperature drops, the corner moves leftward and downward on the image plane. At the end of the test, the horizontal and vertical measurement errors are 0.673 and 5.602 pixels. In other words, the measurement error in the vertical direction is some eight times the counterpart in the horizontal direction. It is also noted that the measurement errors are almost uniform on the whole image plane. Among all the corners, the measurement errors vary between 0.635 and 0.693 pixels in the horizontal direction, and between 5.579 and 5.641 pixels in the vertical direction. It is therefore maintained that the measurement error in the vertical direction is much more significant than its counterpart in the horizontal direction on the image plane. Significant differences in the magnitudes of the measurement errors in the horizontal and vertical directions have also been observed in prior studies (Yu *et al*. 2014, Adamczyk *et al*. 2018, Daakir *et al*. 2019). Nevertheless, the reason behind this is not precisely known yet, which requires further study. Making use of the homography matrix computed in the initial frame, the pixel coordinates of the corner can be transformed to world coordinates and thereby the metric measurement error can be obtained. Correspondingly, it is 0.314 mm in the horizontal direction and 1.860 mm in the vertical direction. It should be noted that the measurement error on the image plane is equally scaled onto the world plane only if the two planes are parallel. Hence, the ratio between vertical and horizontal measurement errors on the world plane usually differs from the counterpart on the image plane. To exemplify this, the measurement error of the (4,6) corner on upper right panel is presented. It is 0.679 pixels or the metric equivalent of 1.237 mm in the horizontal direction, and 5.600 pixels or the metric equivalent of 1.369 mm in the vertical direction. It is apparent that the measurement errors in the horizontal and vertical directions on the world plane get close to each other for this target panel. It is attributed to the fact that the target panel is positioned with a large roll angle relative to the image plane, which is evident in Fig. 1. In this test, the metric measurement error seems to be small. Nevertheless, this is not necessarily the case in field monitoring. The magnitude of metric measurement error also depends on the size of field of view (FOV). It is proportional to the size of FOV in the simplest case where the world plane is parallel to the image plane. The FOV is smaller than 400×400 mm in this test, which may increase substantially in field monitoring as the camera-to-object distance may increase by tens to hundreds times. It is not uncommon to see a scale factor up to tens mm/pixel in field monitoring (Feng and Feng 2017). In addition, the indoor air temperature descended by 10.2°C only in this test. In the continuous monitoring under outdoor environments, the range of the ambient temperature variation may increase by several times. As a result, it is speculated that the measurement error will become intolerable in field monitoring.

To gain an intuitive understanding of the relationship between measurement error and temperature variation, Fig. 5 shows the measurement error vs. the mean temperature of

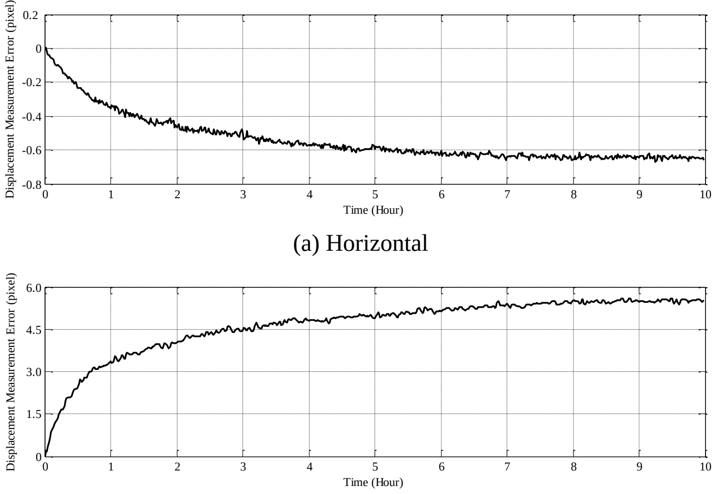

(a) Horizontal

(b) Vertical

Fig. 4 Displacement measurement error of (4,6) corner on upper right target panel in Dataset 1

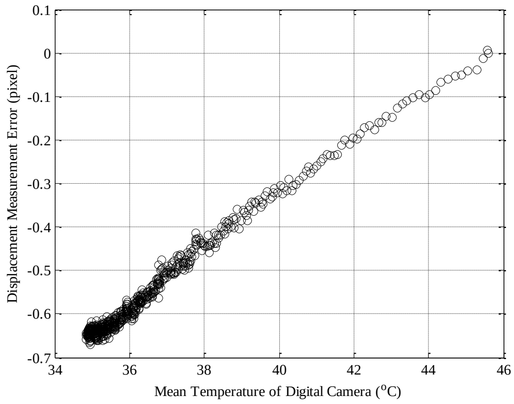

(a) Horizontal

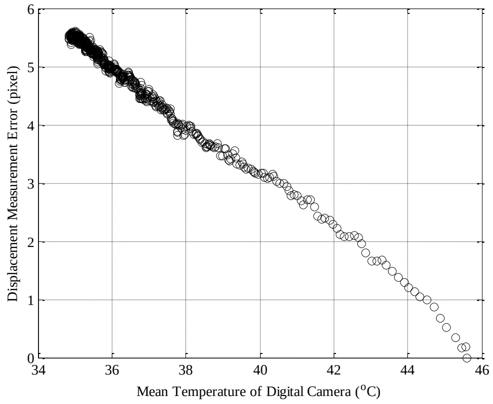

(b) Vertical

Fig. 5 Displacement measurement error vs. mean temperature of digital camera in Dataset 1

Table 2 Regression coefficients and correlation coefficients between measurement errors and temperatures in Dataset 1

Temperature		Horizontal measurement error		Vertical measurement error	
		Slope	Correlation coefficient	Slope	Correlation coefficient
Digital camera	Top	0.064	0.994	-0.475	-0.996
	Bottom	0.064	0.994	-0.478	-0.996
	Left	0.064	0.994	-0.475	-0.996
	Right	0.065	0.994	-0.481	-0.997
	Mean	0.064	0.994	-0.478	-0.996
Zoom lens		0.072	0.992	-0.538	-0.997
Indoor air		0.068	0.990	-0.503	-0.987

digital camera. It is obvious that they generally conform to an excellent linear relationship. To characterize the linear relationship between them, linear regression analyses were carried out and the regression coefficients were obtained by the least-squares method. Meanwhile, the correlation coefficients were calculated as well to quantify the degree of correlation. Table 2 presents the regression coefficients (slopes only) and correlation coefficients between measurement errors and temperatures of vision measurement system as well as indoor air temperature. The correlation coefficients corresponding to the temperatures of the vision measurement system are barely distinguishable for either horizontal or vertical measurement error. All of them are larger than 0.990, indicating that the measurement errors in both directions are completely correlated with the temperatures of vision measurement system. Comparatively speaking, the indoor air temperature is less well correlated with the measurement error. Therefore, it is logical to infer that the measurement error is an outcome attributable to the thermal action on the vision measurement system (digital camera and/or zoom lens). In addition, it is also observed that the correlation coefficients between vertical measurement error and temperature are slightly superior to the counterparts between horizontal measurement error and temperature. It is mainly attributed to the fact that the magnitude of vertical measurement error is much larger than that of horizontal one which helps decrease the discreteness of the linear relationship. Differences are observed in the slopes that correspond to different temperatures. It is ascribed to the different decrements in the temperatures. In this test, the indoor air temperature, mean temperature of digital camera and temperature of zoom lens dropped by 10.2, 10.8 and 9.0°C, respectively.

To examine whether the behavior of the vision measurement system under different temperature variation pattern is the same or not, a second test was performed as the indoor air temperature rises monotonically. The measurement data were denoted as Dataset 2. Fig. 6 presents the measurement error and the mean temperature of digital camera in this test. To be comparable with Dataset 1, the measurement error of the (4,6) corner on central target panel is shown. Satisfactory correspondence between measurement error and mean temperature of digital camera is observed, which implies that they conform to an excellent linear relationship as well. As the temperature ascends, the corner moves rightward and upward on the image plane, which is in line with expectations. In addition, the difference in the magnitudes of the measurement errors in the horizontal and vertical directions is observed again. The vertical measurement error is also some eight times the horizontal one (5.870 vs. 0.772 pixels). Table 3 collects the regression coefficients and correlation coefficients between measurement errors and temperatures of vision measurement system as well as indoor air temperature. As it is seen,

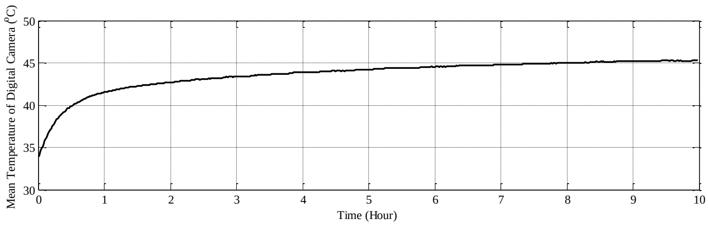

(a) Mean temperature of digital camera

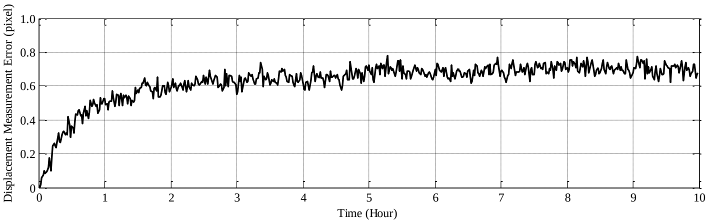

(b) Horizontal measurement error

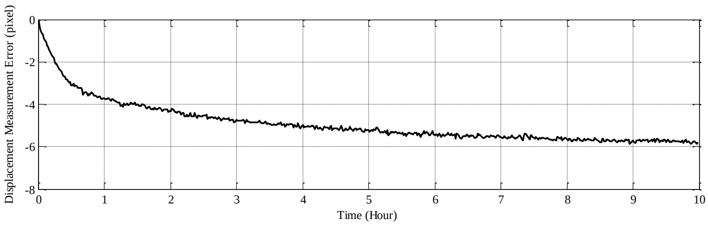

(c) Vertical measurement error

Fig. 6 Displacement measurement error and mean temperature of digital camera in Dataset 2

Table 3 Regression coefficients and correlation coefficients between measurement errors and temperatures in Dataset 2

Temperature		Horizontal measurement error		Vertical measurement error	
		Slope	Correlation coefficient	Slope	Correlation coefficient
Digital camera	Top	0.062	0.954	-0.475	-0.996
	Bottom	0.063	0.954	-0.478	-0.997
	Left	0.062	0.954	-0.476	-0.997
	Right	0.063	0.954	-0.481	-0.995
	Mean	0.062	0.954	-0.478	-0.997
Zoom lens		0.072	0.077	0.948	-0.598
Indoor air		0.068	0.075	0.929	-0.596

the slopes corresponding to temperatures of digital camera are almost the same as their counterparts in Table 2, indicating that the rise and drop in the temperature of digital camera impose nearly the same effect on the videogrammetric displacement monitoring technique. The slopes corresponding to the temperature of zoom lens and indoor air temperature, however, are much larger than their counterparts in Table 2. It is attributed to the fact that the indoor air temperature and the temperature of zoom lens gain smaller increment than temperatures of digital camera when the air conditioner works in heating mode since the digital camera is a heating element itself. In Dataset 2, the indoor air temperature and the mean temperature of digital camera rose by 9.7°C and 11.5°C, resulting in a difference of 1.8°C between them. In contrast, the difference is 0.6°C in Dataset 1. As the slopes corresponding to the temperatures of digital camera are almost the same in the two datasets, it is inferred that the variation of the temperature of digital camera is the main cause of the measurement error. In the perspective of the correlation coefficient between measurement error and temperature, those corresponding to the vertical measurement error change slightly in the two datasets. Nevertheless, the correlation coefficients that correspond to the horizontal one differ notably in the two datasets. Again, it is attributed to the randomness increased by the small magnitude of the horizontal measurement error. In Dataset 2, the correlations between the temperatures themselves are not as good as those in Dataset 1. Consequently, discriminable differences are detected in the correlation coefficients that correspond to different temperatures. Among them, the temperatures of digital camera are most correlated with the measurement error, whether in horizontal or vertical direction. It therefore helps consolidate that the variation of the temperature of digital camera is the main cause of the measurement error. Thereby, it is concluded that the rise and drop in the temperature of digital camera impose nearly the same effect on the videogrammetric displacement monitoring technique. Accordingly, it will be more appropriate to use the temperature of digital camera to formulate the relationship between measurement error and temperature variation.

To examine the behavior of the vision measurement system under cyclic temperature variation as well as the repeatability of the test results obtained in the monotonic temperature variation tests, another test in which the indoor air temperature experienced cyclic fluctuation was performed. The measurement data were denoted as Dataset 3. Fig. 7 displays the measurement error and mean temperature of digital camera in Dataset 3. Again, the measurement error of the (4,6) corner on central target panel is shown. In this test, the temperature of digital camera experienced three rise/drop cycles. Correspondingly, the measurement error, whether in horizontal or vertical direction, also presented three similar cycles of fluctuation. In line with the movement under monotonic temperature variation, the corner moves rightward and upward as the temperature rises and vice versa. The difference in the magnitudes of the measurement errors in the horizontal and vertical directions is also apparent. Furthermore, the mapping between measurement error and mean temperature of digital camera is satisfactory as well. Therefore, it is supposed that the cyclic temperature variation imposes the same effect on the videogrammetric displacement monitoring technique as the monotonic temperature variation does. To evidence this, Table 4 lists the regression coefficients and correlation coefficients between measurement errors and temperatures of digital camera in each cycle of Dataset 3. It is obvious that the slopes between measurement errors (either horizontal or vertical one) and temperatures of digital camera are almost constant in the three cycles, validating the repeatability of the test results. Furthermore, they are almost the same as their counterparts in the monotonic temperature drop/rise tests, which consolidates that the cyclic and monotonic temperature variations impose nearly the same effect on the videogrammetric displacement monitoring technique. In addition, notable differences between the correlation coefficients in different cycles or datasets are detected for the horizontal measurement error, which is also explained by the small magnitude of the horizontal measurement error. In contrast, the correlation coefficients in the three cycles are nearly the same and they are slightly different from the counterparts in monotonic temperature drop/rise tests for the vertical measurement error. On this ground, it is concluded that the monotonic and cyclic temperature variations impose the same effect on the videogrammetric displacement monitoring technique.

4. Temperature-induced variability of camera parameters

In an effort to explore the mechanism responsible for the temperature effect on the videogrammetric displacement

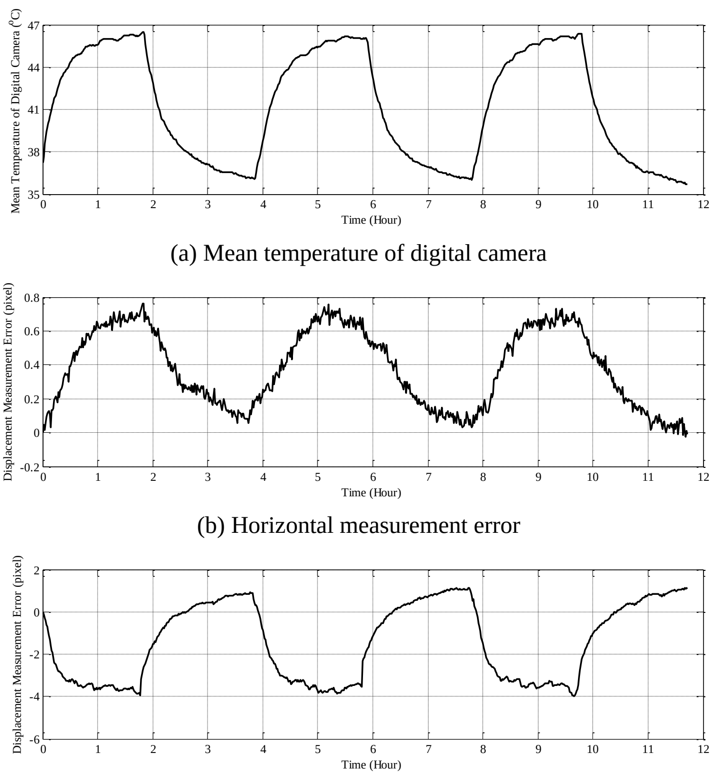

(a) Mean temperature of digital camera

(b) Horizontal measurement error

(c) Vertical measurement error

Fig. 7 Displacement measurement error and mean temperature of digital camera in Dataset 3

Table 4 Regression coefficients and correlation coefficients between measurement errors and temperatures in Dataset 3

Cycle	Temperature of digital camera	Horizontal measurement error		Vertical measurement error	
		Slope	Correlation coefficient	Slope	Correlation coefficient
Cycle 1	Top	0.063	0.962	-0.474	-0.992
	Bottom	0.061	0.958	-0.478	-0.993
	Left	0.063	0.963	-0.475	-0.992
	Right	0.062	0.961	-0.481	-0.993
	Mean	0.062	0.961	-0.477	-0.993
Cycle 2	Top	0.062	0.964	-0.475	-0.994
	Bottom	0.061	0.963	-0.477	-0.993
	Left	0.062	0.964	-0.475	-0.994
	Right	0.062	0.964	-0.481	-0.994
	Mean	0.062	0.964	-0.478	-0.994
Cycle 3	Top	0.063	0.978	-0.475	-0.994
	Bottom	0.062	0.978	-0.477	-0.993
	Left	0.064	0.978	-0.475	-0.994
	Right	0.063	0.978	-0.481	-0.993
	Mean	0.063	0.978	-0.478	-0.994

monitoring technique, an attempt was made to reveal the underlying camera intrinsic and extrinsic parameters and then scrutinize their variability induced by temperature variation. To this end, the homography matrix corresponding to each frame was first computed by making use of the mapping between world coordinates and pixel coordinates of the corners of the checkerboard pattern. The image coordinates of the corners were identified frame by frame with the corner detector proposed by Geiger *et al.* (2012); while their world coordinates remained unchanged in each frame as the target panels were kept fixed in the tests. A minimum of four coplanar points (no three of them are co-linear) are required to compute the homography matrix with the DLT method. To allow for the presence of noise, a total of 49 corners in the central area of the target panel were employed to solve for the homography matrix. After that, the camera intrinsic and extrinsic parameters were estimated from the homography matrices. At a minimum, only three world planes are necessary to solve for the camera parameters with the method developed by Zhang (2000). Again, to allow for the presence of noise, a total of five homography matrices were exploited to extract the camera parameters. As an illustration, the camera parameters extracted from Dataset 3 were presented.

Fig. 8 plots the radial distortion coefficients extracted from Dataset 3. Both of them are non-zero, indicating that lens distortion did occur in this test. Within a temperature range of 10.8°C, they fluctuate randomly around the values computed in the initial frame. It seems to be in conflict with the work done by Poulin-Girard *et al.* (2014), where radial

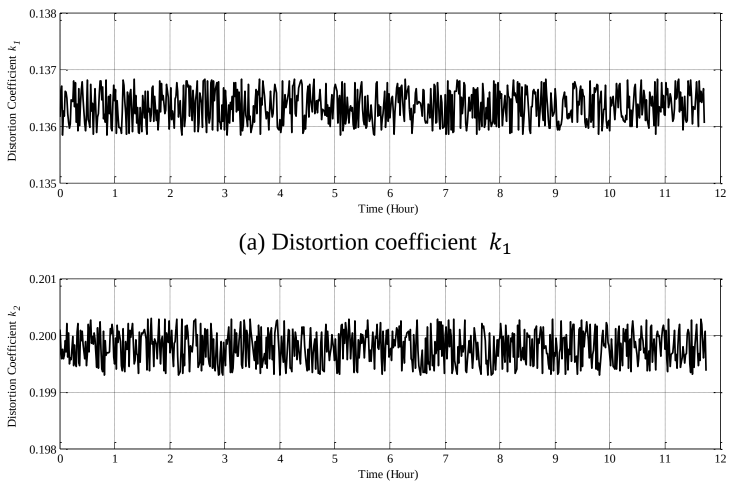

(a) Distortion coefficient k_1

(b) Distortion coefficient k_2

Fig. 8 Radial distortion coefficients extracted from Dataset 3

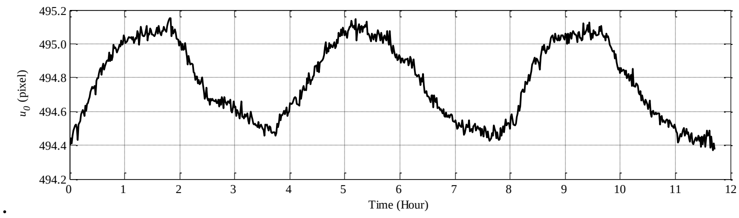

(a) Coordinate of principal point u_0

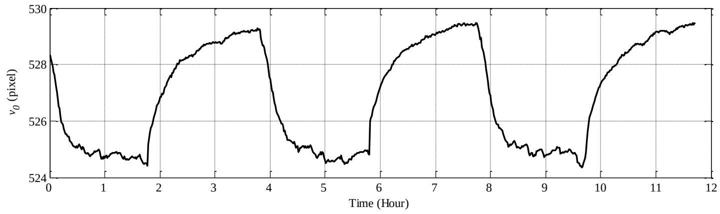

(b) Coordinate of principal point v_0

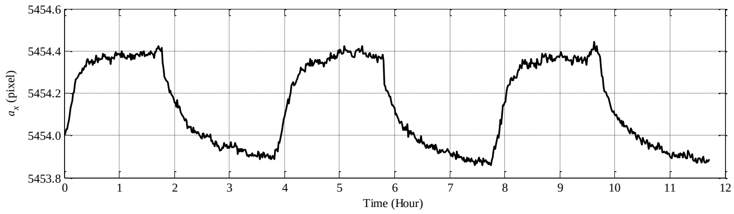

(c) Focal length a_x

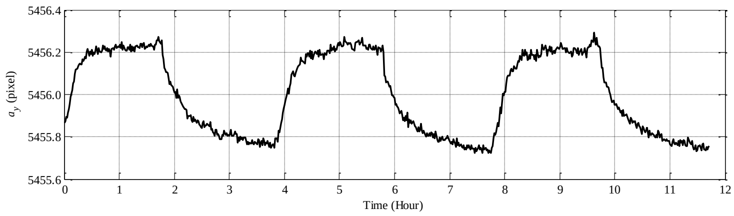

(d) Focal length a_y

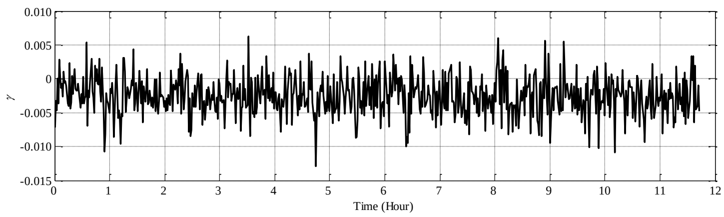

(e) Skew factor γ

Fig. 9 Camera intrinsic parameters extracted from Dataset 3

distortion coefficients showed changes correlated with temperature variation. However, it is worth noting that they showed changes of no more than 0.003 under a temperature range of 500°C. It is therefore speculated that lens distortion is invariant to temperature variation and is unlikely to induce tangible measurement error under varying ambient temperature. Fig. 9 shows the camera intrinsic parameters refined by the correction of lens distortion. Apparent cyclic variations are detected in the camera intrinsic parameters except for the skew parameter. The skew parameter randomly fluctuates around zero, which is in line with expectations as it is usually zero. In other words, the coordinates of principle point and the focal lengths are prone to temperature variation, while the skew parameter is immune to temperature variation. Among them, the variations of the coordinates of principle point are most significant. To exemplify this, the error component caused by the movement of principle point was computed by fixing other camera parameters to the values computed in the initial frame. The results of the four outermost corners as well as the central corner closest to the principle point at the peak temperature are presented in Table 5. The error component arises from the movement of principle point occupies more than 94% and 99% of the total measurement error in the horizontal and vertical directions, respectively. At some corners, it is even larger than the total measurement error, implying that counter effect is generated by other camera parameters. Therefore, it is maintained that the measurement error is an outcome mainly attributed to the variation of the coordinates of principal point. Recalling that the measurement errors are almost uniform on the whole image plane, as exemplified in Dataset 1, it is therefore reasonable to suppose that the movement of principle point is induced by a rigid body motion of the CCD chip (image plane). As per the movements of the corners on the image plane, it can be inferred that the CCD chip moves leftward and downward as the mean temperature of digital camera rises and vice versa. Furthermore, it is also noted that the ratio between vertical and horizontal translations of principal point is very close to the ratio between vertical and horizontal measurement errors. Therefore, the difference in the magnitudes of vertical and horizontal measurement errors is ascribed to the different translations of CCD chip along the two directions. As the interior of digital camera is invisible, the reason for the different translations of CCD chip in the two directions is not precisely known yet. It is suspected to be a result of the non-uniform thermal deformation of the support of CCD chip. In the future work, efforts will be made to reveal the interior of digital camera.

As far as the focal lengths are concerned, both of them increase as the temperature of digital camera rises and vice versa. In comparison with the variation of the coordinates of principal point, the variation of focal lengths is much smaller in magnitude. Accordingly, the error component caused by the variation of focal lengths may be smaller. Table 6 lists the statistics of the error component induced by the variation of focal lengths at the peak temperature. It is seen that the proportion of the error component produced by the variation of focal lengths in the total measurement error is generally no more than 5%, whether in horizontal or vertical direction. In this sense, the error component generated by the variation of focal lengths can be thought of as trivial in most cases unless an extremely high accuracy is required. It is also observed that the corners on the top move upward while the corners on the bottom move downward on the image plane. Likewise, the corners on the left and those on the right move in opposite direction on the image plane. Meanwhile, the error component due to the variation of focal lengths is nearly zero at the central corner. So more succinctly, the corners move outward (except for the principal point) as the focal length increases and vice versa. This squares with the fact. As per the central projection principle, the object expands on the image plane as the focal length elongates, which is equivalent to the outward movements of the corners on the image plane. Recalling Table 5, it is found that the error component induced by the variation of focal lengths is contrary to the counterpart caused by the variation of the coordinates of principal point at some corners. It is explained by the fact that the variation of focal lengths makes the corners move inward/outward on the image plane, whereas the variation of the coordinates of principal point leads to uniform movements of the corners on the whole image plane. Consequently, the error component induced by the movement of principle point is larger than the total measurement error at these corners.

To gain a direct perception of the temperature-induced variability of the camera extrinsic parameters, the variations of the Euler angles and translation components of the bottom right target panel are plotted in Figs. 10 and 11, respectively. It is evident that only the roll angle and camera-to-object distance show variations well correlated with temperature, whereas the rest parameters are independent of temperature variation. Recalling Fig. 7(a), it can be seen that the camera-to-object distance decreases as the mean temperature of digital camera rises and vice versa. It shows a good agreement with the fact that the digital camera and/or zoom lens expand as the temperature ascends which thereby shortens the camera-to-object distance. Though the camera-to-object distance varies in a small range only, it shows a good correspondence with the mean

Table 5 Statistics of error component due to movement of principle point at peak temperature in Dataset 3

Corner	Total measurement error		Error component		Proportion of error component	
	Horizontal	Vertical	Horizontal	Vertical	Horizontal	Vertical
Upper left	0.640	3.909	0.675	3.944	105.4	100.9
Upper right	0.711	3.913	0.675	3.944	95.0	100.8
Bottom left	0.640	3.972	0.675	3.944	105.6	99.3
Bottom right	0.717	3.968	0.675	3.944	94.1	99.4
Central	0.675	3.944	0.675	3.944	100.0	100.0

Table 6 Statistics of error component due to variation of focal lengths at peak temperature in Dataset 3

Corner	Total measurement error		Error component		Proportion of error component	
	Horizontal	Vertical	Horizontal	Vertical	Horizontal	Vertical
Upper left	0.640	3.909	-0.030	-0.031	-4.8	-0.8
Upper right	0.711	3.913	0.032	-0.027	4.5	-0.7
Bottom left	0.640	3.972	-0.031	0.024	-4.9	0.6
Bottom right	0.717	3.968	0.037	0.020	5.1	0.5
Central	0.675	3.944	0	0	0.0	0.0

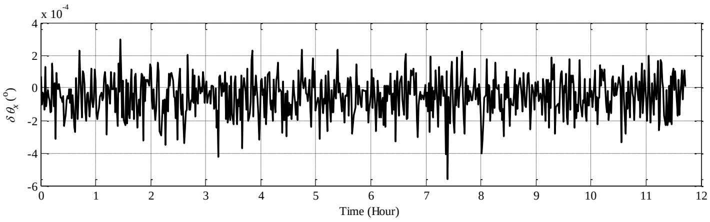

(a) Pitch angle

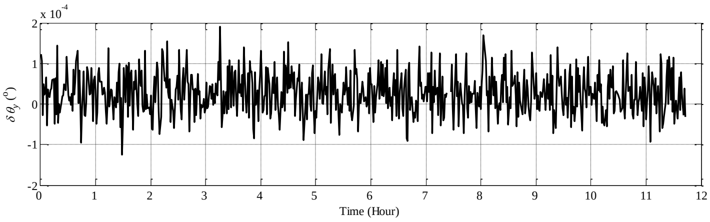

(b) Yaw angle

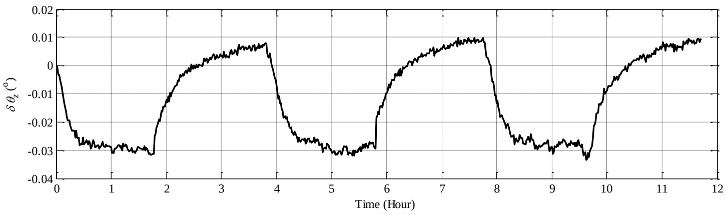

(c) Roll angle

Fig. 10 Changes in Euler angles of bottom right target panel in Dataset 3

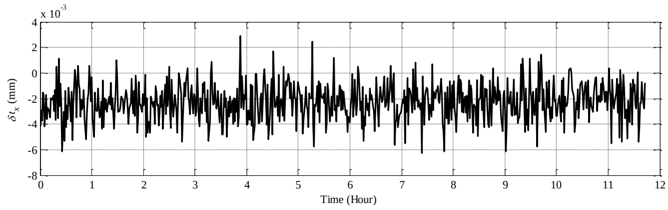

(a) x-component

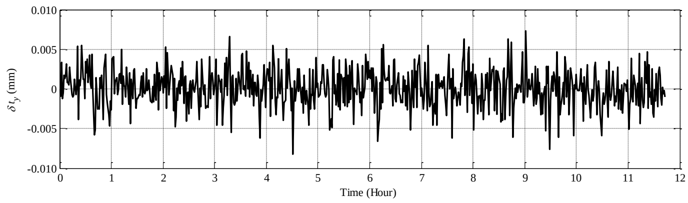

(b) y-component

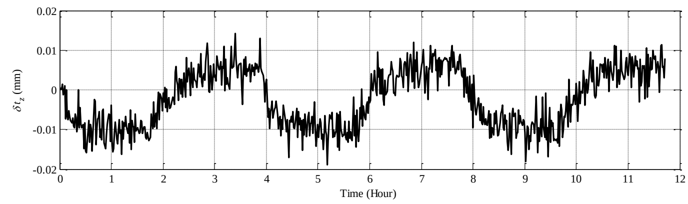

(c) z-component

Fig. 11 Changes in translation components of bottom right target panel in Dataset 3

temperature of digital camera. It therefore helps verify the correctness of the extracted camera parameters. As the target panels were kept fixed throughout the tests, only minor pose variations are observed. To exemplify this, Table 7 shows the comparisons of the pose of all the five target panels computed at reference temperature and peak

Table 7 Pose of target panels computed at reference temperature and peak temperature in Dataset 3

Corner	Reference temperature						Peak temperature					
	θ_x	θ_y	θ_z	t_x	t_y	t_z	θ_x	θ_y	θ_z	t_x	t_y	t_z
Upper left	-5.770	31.196	50.664	-93.475	94.162	1826.381	-5.770	31.196	50.635	-93.479	94.170	1826.365
Upper right	5.387	-33.479	-50.855	105.336	92.653	1790.108	5.387	-33.479	-50.884	105.333	92.661	1790.092
Bottom left	21.552	32.845	33.110	-92.969	-96.665	1832.423	21.552	32.845	33.081	-92.969	-96.657	1832.407
Bottom right	-7.322	-30.533	12.932	101.917	-90.572	1775.712	-7.322	-30.533	12.904	101.915	-90.564	1775.695
Central	5.246	30.906	1.706	-0.382	-5.094	1713.686	5.246	30.906	1.678	-0.389	-5.086	1713.669

temperature. Among the Euler angels, the roll angle shows the most remarkable variation. A maximum variation of 0.030^o is observed in the roll angle of the right bottom target panel. Likewise, the camera-to-object distance exhibits the most significant variation among the translation components. The maximum variation, which is 0.017 mm, is occurred in the central target panel. It is therefore expected that the measurement error induced by the variation of camera extrinsic parameters will be negligible. Actually, such is the fact. To evidence this, the error component induced by the variation of Euler angles or translation vector was calculated. To save space, the detailed results are not presented. Among the four outermost corners as well as the central corner, the error component results from the variation of Euler angels does not contribute to the total measurement error in the vertical direction, and it occupies no more than 0.2% in the horizontal direction. Likewise, the error component arises from the variation of translation vector accounts for less than 0.6% and 0.1% of the total measurement error in the horizontal and vertical directions. Recognizing that the camera-to-object distance in this test is some 1,800 mm only, the relative variation of the camera-to-object distance will become more trivial in field monitoring as its initial length will increase substantially. Therefore, it is speculated that the error component due to the variation of translation vector will contribute less in the total measurement error in field monitoring. Thereby, it is believed that the camera extrinsic parameters are insensitive to temperature variation and their contributions to the total measurement error are negligible.

5. Elimination of temperature-caused measurement error

Making use of the temperature-induced variability of the camera parameters revealed in this study, an approach is proposed for eliminating the temperature-caused measurement error in videogrammetric displacement measurements. First, correlation models between camera parameters and temperature are formulated. Among the camera parameters, the coordinates of principle point and the focal lengths are shown to be prone to temperature variation. Accordingly, correlation models are individually established for them. To this end, camera calibration tests are needed to be conducted before field monitoring to obtain measurement data for model fitting. The variation of the coordinates of principle point due to temperature variation is inherent to the camera itself. Therefore, it is invariant to the measurement setup and thereby the correlation model between coordinates of principle point and temperature is applicable to different measurement setups. Nevertheless, the focal length is dependent on the measurement setup if zoom lens is utilized. In other words, the initial value of focal length differs in different measurement setups. So far, the relationship between focal length and temperature under different initial focal lengths has not been studied. To reduce the uncertainties that may be induced by the different initial values of focal length, it is desirable to set the focal length in the camera calibration test the same as the one to be used in field monitoring. It can be fulfilled by scaling down the FOV according to the ratio between the camera-to-object distances used in field monitoring and camera calibration test. In this study, linear correlation models are constructed by means of linear regression analysis thanks to the excellent linear relationship between them. Given a set of temperature data measured in field monitoring, the corresponding coordinates of principle point and focal lengths are then predicted from the correlation models. After that, the camera projective matrix or homography matrix is updated using the predicated camera parameters in conjunction with other in-situ calibrated camera parameters. Finally, the temperature-caused measurement error can be eliminated by reconstructing the world coordinates of the target with the measured pixel coordinates and the updated camera projective matrix or homography matrix.

As an illustration, the elimination of the temperature-caused measurement error in Dataset 3 is elaborated herein. The measurement data are divided into two subsets. The measurement data in the first cycle are employed for model fitting, which constitutes the training data set. The measurement data in the succeeding two cycles are exploited for model testing, which constitutes the testing data set. Making use of the mean temperature of digital camera and the corresponding camera parameters in the training data set, linear correlation models are formulated for the coordinates of principle point and the focal lengths by linear regression analysis. After that, the temperature data in the training data set are fed into the models again to generate reproduced camera parameters to evaluate the reproduction capability of the models. Likewise, the temperature data in the testing data set are presented to the models to output predicted camera parameters to assess the prediction capability. To quantify the model performance, residuals between measured and reproduced/predicted camera parameters as well as correlation coefficients

Table 8 Statistics of reproduced and predicted camera parameters in Dataset 3

Camera parameters	Range	RMS of residuals		Correlation coefficient	
		Reproduced	Predicted	Reproduced	Predicted
u_0	0.799	0.054	0.053	0.967	0.969
v_0	5.061	0.172	0.212	0.995	0.992
a_x	0.585	0.025	0.029	0.994	0.990
a_y	0.568	0.022	0.029	0.993	0.989

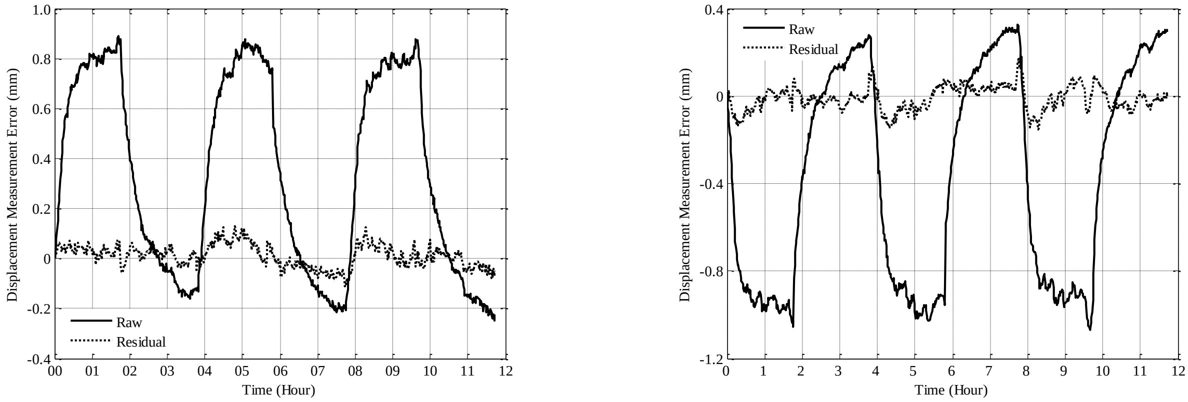

(a) Horizontal (b) Vertical

Fig. 12 Raw and residual measurement error of bottom left corner in Dataset 3

Table 9 RMS of raw and residual measurement errors in Dataset 3

Corner	Raw error		Residual error considering variation of focal lengths		Residual error neglecting variation of focal lengths	
	Horizontal	Vertical	Horizontal	Vertical	Horizontal	Vertical
Upper left	0.760	0.421	0.051	0.038	0.052	0.039
Upper right	0.553	0.674	0.052	0.045	0.053	0.046
Bottom left	0.599	0.689	0.047	0.060	0.048	0.061
Bottom right	0.358	0.814	0.025	0.065	0.026	0.066
Central	0.205	0.862	0.019	0.066	0.019	0.066

between them are calculated. Table 8 summarizes the statistics of the reproduced and predicted camera parameters. As it can be seen, the models achieve comparable reproduction and prediction performance in terms of both RMS of residuals and correlation coefficient. In general, the residuals are deemed small relative to the fluctuation range of the camera parameters. It illustrates that the models possess satisfactory reproduction and prediction capabilities, which can also be validated in the perspective of the correlation coefficient. All the correlation coefficients are larger than 0.96 and most of them approach up to 0.99.

Making use of the reproduced or predicted camera parameters (the coordinates of principal point and the focal lengths) along with other camera parameters computed in the initial frame, the corresponding homography matrix is updated. The world coordinates of the corners are reconstructed from their pixels coordinates with the use of the updated homography matrix. With reference to the world coordinates of the corners in the initial frame, the displacements are then computed. As the target panels were kept fixed in the test, the displacement is purely the residual measurement error obtained after the removal of the error components arises from the variations of coordinates of principle point and focal lengths. As an illustration, Fig. 12 presents the comparisons between raw and residual measurement errors of the bottom left corner. The residual measurement error fluctuates in a small range only, which shows no apparent correlations with temperature variation. In addition, the measurement error rectified by predicted camera parameters is not inferior to the counterpart rectified by reproduced camera parameters, thanks to the comparable reproduction and predication capabilities of the formulated correlation models. It indicates that the approach is competent for eliminating the temperature-caused measurement error. Table 9 collects the RMS of raw and residual measurement errors. It is apparent that the magnitude of the measurement error reduces substantially after the elimination of temperature effect. The RMS of residual measurement error is no more than 10% of the RMS of raw measurement error, whether in horizontal or vertical direction. It therefore verifies that the approach achieves satisfactory performance for eliminating temperature-caused measurement error. It is expected that better performance can be achieved by the approach in field monitoring as the temperature sensitive error components will occupy more share when the temperature range increases.

Recalling that the error component results from the variation of focal lengths occupies a small share in the total measurement error, an attempt is also made to rectify the raw measurement error with the use of updated coordinates of principal point only. The results are also shown in Table 9. It is evident that the RMSs of residual measurement errors obtained by the two means are barely discriminable, implying that only trivial improvement is achieved at the price of more complex computations. It is therefore speculated that it may be unnecessary to take account of the variation of focal length in the elimination of the temperature-caused measurement error. On this premise, an alternative approach for eliminating temperature-caused measurement error can be employed. First, correlation models between coordinates of principle point and temperature are formulated in a similar way. To eliminate the temperature effect, the pixel coordinates of the target under different temperature conditions are then normalized to the reference status of temperature in the initial frame by making use of the correlation models. Specifically, the coordinates of principal point that corresponds to the reference temperature is obtained from the models by feeding the reference temperature into it. Likewise, the coordinates of principal point corresponding to temperatures other than the reference temperature are predicted from the models in the same way. Hereof, the temperature-caused change in the coordinates of principal point can be obtained by subtracting the reference coordinates of principal point from the predicted counterparts. The normalized pixel coordinates of the target are finally obtained by subtracting the temperature-caused change of the coordinates of principal point from the measured pixel coordinates of the target. After that, the world coordinates of the target are computed from the normalized pixel coordinates of the target, in which the temperature-caused measurement error are removed, with the use of the camera projective matrix or homography matrix computed in the initial frame. This approach is also examined by Dataset 3. The results are almost the same as those presented in Table 9 expect for some trivial differences caused by numerical computation. To save space, the detail results are not presented. An advantage to neglect the variation of focal length is that the focal length in the camera calibration test is not necessarily set into the one to be used in the field monitoring. It will significantly facilitate the camera calibration test and thereby enhance the general validity of the proposed approach. Therefore, the approach is believed to have wide applicative perspectives in real applications.

6. Conclusions

The effect of temperature variation on the videogrammetric displacement measurement has been investigated in this study. Camera calibration tests have been performed under both monotonic and cyclic air temperature variations. Features of measurement error and the casual link between temperature variation and measurement error have been revealed. The underlying camera intrinsic and extrinsic parameters have been extracted and their temperature-induced variability has been examined. By so doing, the mechanism responsible for the temperature effect of the videogrammetric technique has been explored. On this ground, an approach for eliminating the temperature-caused measurement error in videogrammetric displacement measurements has been proposed. The performance of the approach for eliminating the temperature-caused measurement error has been examined by making use of the measurement data acquired under cyclic temperature variation. The following conclusions have been drawn from this study:

- The monotonic and cyclic air temperature variations impose nearly the same effect on the videogrammetric displacement measurement technique. The variation of the temperature of digital camera is identified as the main cause of measurement error. An excellent linear relationship between measurement error and mean temperature of digital camera is observed.
- Among the camera parameters, the coordinates of principle point and the focal lengths are prone to temperature variation, whereas the rest of them are insensitive to temperature variation. Both the coordinates of principle point and the focal lengths show variations well correlated with temperature variation, which is of great value for the elimination of temperature-caused measurement error.
- Different camera parameters impose counter effect on the total measurement error. The error component arises from the variation of the coordinates of principle point accounts for a dominantly large percentage in the total measurement error, whereas the proportion of the error component results from the variation of the focal lengths is small. The measurement error is therefore thought to be an outcome mainly attributed to the variation of the coordinates of principle point.
- The proposed approach for eliminating the temperature-caused measurement error in videogrammetric displacement measurements achieves satisfactory performance. Taking account of the variation of the focal length barely improves the performance of the approach. A simplified approach without considering the variation of the focal length may be sufficient for eliminating the temperature-caused measurement error, which helps enhance the general validity of the approach.

Acknowledgments

The author(s) disclosed receipt of the following financial support for the research, authorship and/or publication of this article: This research was supported in part by grants from the National Natural Science Foundation of China (Project No. 51578424, 51208384), a grant from the Science Technology Department of Zhejiang Province, China (Project No. 2012R10071), a grant from Wenzhou Science and Technology Bureau, China (Project No. S20150018), and a grant from the Zhejiang Provincial National Science Foundation of China (Project No. LY12E08009).

References

Abdel-Aziz, Y.I. and Karara, H.M. (2015), "Direct linear transformation from comparator coordinates into object-space coordinates in close-range photogrammetry", *Photogrammetric Eng. Remote Sensing*, **81**, 103-107. https://doi.org/10.14358/PERS.81.2.103

Adamczyk, M., Liberadzki, P. and Sitnik, R. (2018), "Temperature Compensation Method for Digital Cameras in 2D and 3D Measurement Applications", *Sensors*, **18**(11), 3685. https://doi.org/10.3390/s18113685

Baqersad, J., Poozesh, P., Niezrecki, C. and Avitabile, P. (2017), "Photogrammetry and optical methods in structural dynamics – A review", *Mech. Syst. Signal Process.*, **86**, 17-34. https://doi.org/10.1016/j.ymssp.2016.02.011

Brownjohn, J.M.W., Xu, Y. and Hester, D. (2017), "Vision-based bridge deformation monitoring", *Front. Built Environ.*, **3**, 23. https://doi.org/10.3389/fbuil.2017.00023

Busca, G., Cigafa, A., Mazzoleni, P. and Zappa, E. (2014), "Vibration monitoring of multiple bridge points by means of a unique vision-based measuring system", *Experim. Mech.*, **54**, 255-271. https://doi.org/10.1007/s11340-013-9784-8

Chang, C.C. and Xiao, X.H. (2010), "An integrated visual-inertial technique for structural displacement and velocity measurement", *Smart Struct. Syst., Int. J.*, **6**(9), 1025-1039. https://doi.org/10.12989/sss.2010.6.9.1025

Chatterjee, C. and Roychowdhury, V.P. (2000), "Algorithms for coplanar camera calibration", *Mach. Vision Applicat.*, **12**, 84-97. https://doi.org/10.1007/s001380050127

Cho, S., Lee, J. and Sim, S.H. (2018), "Comparative study on displacement measurement sensors for high-speed railroad bridge", *Smart Struct. Syst., Int. J.*, **21**(5), 637-652. https://doi.org/10.12989/sss.2018.21.5.637

Daakir, M., Zhou, Y., Deseilligny, M.P., Thom, C., Martin, O. and Rupnik, E. (2019), "Improvement of photogrammetric accuracy by modeling and correcting the thermal effect on camera calibration", *ISPRS J. Photogrammetry Remote Sensing*, **148**, 142-155. https://doi.org/10.1016/j.isprsjprs.2018.12.012

Faugeras, O.D. and Toscani, G. (1986), "The calibration problem for stereo", *Proceedings of the IEEE Conference on Computer Vision and Pattern Recognition*, IEEE, New York, USA.

Feng, D.M. and Feng, M.Q. (2016), "Vision-based multipoint displacement measurement for structural health monitoring", *Struct. Control Health Monitor.*, **23**, 876-890. https://doi.org/10.1002/stc.1819

Feng, D.M. and Feng, M.Q. (2017), "Experimental validation of cost-effective vision-based structural health monitoring", *Mech. Syst. Signal Process.*, **88**, 199-211. https://doi.org/10.1016/j.ymssp.2016.11.021

Feng, D.M. and Feng, M.Q. (2018), "Computer vision for SHM of civil infrastructure: From dynamic response measurement to damage detection – A review", *Eng. Struct.*, **156**, 105-117. https://doi.org/10.1016/j.engstruct.2017.11.018

Geiger, A., Moosmann, F., Car, Ö. and Schuster, B. (2012), "Automatic camera and range sensor calibration using a single shot", *Proceedings of 2012 IEEE International Conference on Robotics and Automation*, IEEE, New York, USA.

Handel, H. (2009), "Analyzing the influences of camera warm-up effects on image acquisition", *IPSJ Transact. Comput. Vision Applicat.*, **1**, 12-20. https://doi.org/10.1007/978-3-540-76390-1_26

Jiang, R.N., Jáuregui, D.V. and White, K.R. (2008), "Close-range photogrammetry applications in bridge measurement: Literature review", *Measurement*, **41**, 823-834. https://doi.org/10.1016/j.measurement.2007.12.005

Lee, J.J., Fukuda, Y., Shinozuka, M., Cho, S.J. and Yun, C.B. (2007), "Development and application of a vision-based displacement measurement system for structural health monitoring of civil structures", *Smart Struct. Syst., Int. J.*, **3**(3), 373-384. https://doi.org/10.12989/sss.2007.3.3.373

Lee, J.H., Ho, H.N., Shinozuka, M. and Lee, J.J. (2012), "An advanced vision-based system for real-time displacement measurement of high-rise buildings", *Smart Mater. Struct.*, **21**, 125019. https://doi.org/10.1088/0964-1726/21/12/125019

Lee, J.H., Jung, C.Y., Choi, E. and Cheung, J.H. (2017), "Vision-based multipoint measurement systems for structural in-plane and out-of-plane movements including twisting rotation", *Smart Struct. Syst., Int. J.*, **20**(5), 563-572. https://doi.org/10.12989/sss.2017.20.5.563g

Liu, T.S., Burner, A.W., Jones, T.W. and Barrows, D.A. (2012), "Photogrammetric techniques for aerospace applications", *Progress Aerosp. Sci.*, **54**, 1-58. https://doi.org/10.1016/j.paerosci.2012.03.002

Merchant, D.C. (2006), "Influence of Temperature on Focal Length for the Airborne Camera", *Proceedings of San Antonio 2006 ASPRS-MAPPS Fall Conference*, San Antonio, TX, USA.

Olaszek, P. (1999), "Investigation of the dynamic characteristic of bridge structures using a computer vision method", *Measurement*, **25**, 227-236. https://doi.org/10.1016/S0263-2241(99)00006-8

Podbreznik, P. and Potočnik, B. (2012), "Assessing the influence of temperature variations on the geometrical properties of a low-cost calibrated camera system by using computer vision procedures", *Mach. Vision Applicat.*, **23**, 953-966. https://doi.org/10.1007/s00138-011-0330-3

Poulin-Girard, A.S., Dallaire, X., Veillette, A., Thibault, S. and Laurendeau, D. (2014), "Study of camera calibration process with ray tracing", In: *Current Developments in Lens Design and Optical Engineering XV, Proceedings of SPIE*, (R.B. Johnson, V.N. Mahajan, S. Thibault Eds.), Vol. 9192, SPIE Press, Bellingham, WA, USA.

Robson, S., Clarke, T.A. and Chen, J. (1993), "The suitability of the Pulnix TM6CN CCD camera for photogrammetric measurement", In: *Videometrics II, Proceedings of SPIE*, (S.F. El-Hakim Ed.), Vol. 2067, SPIE Press, Bellingham, WA, USA.

Salvi, J., Armangué, X. and Batlle, J. (2002), "A comparative review of camera calibrating methods with accuracy evaluation", *Pattern Recognit.*, **35**, 1617-1635. https://doi.org/10.1016/S0031-3203(01)00126-1

Sharpe Jr., W.N. (2008), *Handbook of experimental solid mechanics*, Springer US, New York, USA.

Smith, M.J. and Cope, E. (2010), "The effects of temperature variation on single-lens-reflex digital camera calibration parameters", *International Archives of Photogrammetry, Remote Sensing and Spatial Information Sciences*, **38** (Part 5), 554-559.

Sun, W. and Cooperstock, J.R. (2006), "An empirical evaluation of factors influencing camera calibration accuracy using three publicly available techniques", *Mach. Vision Applicat.*, **17**, 51-67. https://doi.org/10.1007/s00138-006-0014-6

Surhone, L.M., Tennoe, M.T. and Henssonow, S.F. (2010), *Videogrammetry*, Betascript Publishing.

Tsai, R.Y. (1987), "A versatile camera calibration technique for high-accuracy 3D machine vision metrology using off-the-shelf TV cameras and lenses", *IEEE J. Robotics Automat.*, **3**, 323-344. https://doi.org/10.1109/JRA.1987.1087109

Wahbeh, A.M., Caffrey, J.P. and Masri, S.F. (2003), "A vision-based approach for the direct measurement of displacements in vibrating systems", *Smart Mater. Struct.*, **12**, 785-794. https://doi.org/10.1088/0964-1726/12/5/016

Weng, J., Cohen, P. and Herniou M. (1992), "Camera calibration with distortion models and accuracy evaluation", *IEEE Transact. Pattern Anal. Mach. Intel.*, **14**, 965-980. https://doi.org/10.1109/34.159901

Widenhorn, R., Blouke, M.M., Weber, A., Rest, A. and Bodegom, E. (2002), "Temperature dependence of dark current in a CCD", In: *Sensors and Camera Systems for Scientific, Industrial, and Digital Photography Applications III, Proceedings of SPIE*, (N. Sampat, M.M. Blouke, J. Canosa Eds.), Vol. 4669, SPIE Press, Bellingham, WA, USA.

Xu, Y. and Brownjohn, J.M.W. (2018), "Review of machine-vision based methodologies for displacement measurement in civil structures", *J. Civil Struct. Health Monitor.*, **8**, 91-110. https://doi.org/10.1007/s13349-017-0261-4

Yu, Q.F., Chao, Z.C., Jiang, G.W., Shang, Y., Fu, S.H., Liu, X.L., Zhu, X.W. and Liu, H.B. (2014), "The effects of temperature variation on videometric measurement and a compensation method", *Image Vision Comput.*, **32**, 1021-1029. https://doi.org/10.1016/j.imavis.2014.08.011

Zhang, Z.Y. (2000), "A flexible new technique for camera calibration", *IEEE Transact. Pattern Anal. Mach. Intel.*, **22**, 1330-1334. https://doi.org/10.1109/34.888718

Zhou, H.F., Zheng, J.F., Xie, Z.L., Lu, L.J., Ni, Y.Q. and Ko, J.M. (2017), "Temperature effects on vision measurement system in long-term continuous monitoring of displacement", *Renew. Energy*, **114**, 968-983. https://doi.org/10.1016/j.renene.2017.07.104

Zhou, H.F., Lu, L.J., Li, Z.Y. and Ni, Y.Q. (2019), "Performance of videogrammetric displacement monitoring technique under varying ambient temperature", *Adv. Struct. Eng.*, **22**(16), 3371-3384. https://doi.org/10.1177/1369433218822089

BS